Article

Quantitative Evaluation of Bathymetric LiDAR Sensors and Acquisition Approaches in Lærdal River in Norway

Mahmoud Omer Mahmoud Awadallah [1,2,*] **, Christian Malmquist** [3,4] **, Morten Stickler** [5,6] **and Knut Alfredsen** [1]

1 Department of Civil and Environmental Engineering, Norwegian University of Science and Technology, 7031 Trondheim, Norway

2 Laboratory of Hydraulics, Hydrology and Glaciology, Department of Civil, Environmental and Geomatic Engineering, ETH Zürich, 8093 Zürich, Switzerland

3 Department of Marine Technology, Norwegian University of Science and Technology, 7031 Trondheim, Norway

4 The Norwegian Mapping Authority, 8003 Bodø, Norway

5 The Norwegian Water Resources and Energy Directorate, 0301 Oslo, Norway

6 Department of Natural Sciences and Environmental Health, The University of South East Norway, 3800 Bø, Norway

* Correspondence: mahmoud.awadallah@ntnu.no

Abstract: The development of bathymetric LiDAR technology has contributed significantly to both the quality and quantity of river bathymetry data. Although several bathymetric LiDAR sensors are available today, studies that evaluate the performance of the different bathymetric LiDAR sensors comparatively are still lacking. This study evaluates the performance of three bathymetric LiDAR sensors, CZMIL Supernova, Riegl VQ880-G, and Riegl VQ840-G, used with different acquisition approaches, in mapping Lærdal River bathymetry in Norway. The performance was evaluated based on comparing the sensors against a multibeam echosounder (MBES), a terrestrial laser scanner (TLS), and by an intercomparison between the individual sensors. The comparison was completed by comparing point clouds from the instruments and through the comparison of DEMs created from the point clouds. For the comparison against the MBES, the results show that the median residuals range between 3 to 13 cm, while against the TLS the median residuals range between 0 to 5 cm. The comparison of the CZMIL sensor against the two Riegl sensors shows median residuals of around 12 cm where the CZMIL map is shallower against the VQ880-G and deeper against the VQ840-G sensor. For the two Riegl sensors, the results show a median difference of 2 cm with the VQ880-G map deeper. We do observe that areas with high residuals are linked to river features such as large substrate variability, steep banks, and whitewater/turbulent flow. The study shows that all the LiDAR instruments provide high-quality representations of the river geometry and create a solid foundation for planning, modelling, or other work in rivers where detailed bathymetry is needed.

Keywords: river bathymetry; airborne bathymetric LiDAR; ALB; LiDAR; topo-bathymetric; LiDAR acquisition

1. Introduction

Detailed river bottom geometry, commonly referred to as bathymetry, is a key factor within river management for studying a wide range of societal applications such as flood risk and climate mitigation, sediment transport and erosion, and ecosystem studies [1–4]. Bathymetric data collection has traditionally been conducted using differential global positioning system (GPS) and total stations in shallow wadable rivers and multibeam technology in deep non-wadable river sections [5–8]. However, applying such conventional methods for bathymetric surveys can be associated with many challenges ranging from health, safety, and environmental risks (HSE) associated with accessing the river, costs related to time used in the field, and high economic costs [5,9–11]. The emergence of

remote sensing technology, however, has been a quantum leap in the field of bathymetry acquisition that resolves the majority of the ground survey challenges [12–14].

Light detection and ranging (LiDAR) technology is one of the recent popular sources for river geometry acquisition that enables rapid and accurate 3D point cloud collection. The technology measures the distance to a target by detecting the time between the emission of a pulse of laser from a sensor and the time of detection of the reflected laser from the target [15]. Depending on the wavelength, two types of LiDAR sensors exist: topographic LiDAR and bathymetric LiDAR. Topographic LiDAR is associated with a laser of 1064 nm that is unable to penetrate water bodies and therefore used mostly for topographic surface detection. Bathymetric LiDAR, on the other hand, is commonly characterized by a laser of 532 nm that penetrates the water and gives bottom detection [16]. The bathymetric LiDAR is the most widespread LiDAR type used in river studies that require high degrees of mapping accuracy such as environmental river studies [17–19], sediment transport studies [20,21], and flood modelling [22,23].

Today, a variety of bathymetric LiDAR sensors are commercially available, each defined by their technical specifications such as the laser energy per pulse, the laser footprint, and the maximum detectable depth. The question of which sensor is most suitable for bathymetric mapping will primarily depend on project objectives, physical features of the area of interest such as water depths, river gradient and water turbidity, and sensor availability [24]. The Teledyne Optech CZMIL (Coastal Zone Mapping and Imaging LiDAR), for instance, is an airborne multi-sensor used for mapping topographic surfaces and coastal zones [25–27], and the high laser energy per pulse characteristic makes it suitable to map deep depths such as those in the coastal applications [26,28]. However, the high laser penetration in the CZMIL comes at the point density cost since the laser energy and the point density are negatively correlated [24]. Riegl VQ880-G, on the other hand, is an airborne topo-bathy sensor with lower laser energy per pulse and a smaller footprint, compared to the CZMIL, that can map with much higher point density but less water penetration [21,24,29]. Riegl VQ840-G is another topo-bathy sensor that is much lighter than the common bathymetric LiDAR sensors' weight and, therefore, can be operated from an unmanned aerial vehicle or helicopters [30,31].

The evaluation of the performance of bathymetric LiDAR sensors is an important aspect within both coastal [28,32] and shallow fluvial mapping [3,21,30,33–35], especially when a high degree of accuracy is crucial such as for ecological assessment. In coastal applications, Costa et al. (2009) [28] have evaluated the performance of the Laser Airborne Depth Sounder (LADS) Mk II Airborne System in providing benthic habitat maps compared to ship-based multibeam (MBES) Sound Navigation and Ranging (SoNAR) at the western coast of Puerto Rico. Cost and mapping-wise, they have found that the bathymetric LiDAR works as an efficient alternative to the MBES in mapping and monitoring shallow water coral reef ecosystems at less than 50 m deep. In the fluvial mapping, many studies have evaluated the performance of different bathymetric LiDAR sensors deployed on airborne such as Aquarius [33,36], EAARL and EAARL-B [3,34,35], Lieca Chiroptera II [37,38], and Riegl VQ880-G [21,39], and sensors deployed on drone such as Riegl VQ840-G [30], ASRTALiTe EDGE [40], and TDOT GREEN [41]. Fernandez-Diaz et al. (2014) [33] and Legleiter et al. (2016) [36] have evaluated the performance of the Aquarius sensor against DGPS and the Analytical Spectral Device (ASD) in mapping both clear and turbid rivers and reported a root mean square error (RMSE) of 0.13 m in a clear river and 0.24 m in a relatively turbid river. The studies of Kinzel et al. (2013) [3] and Tonina et al. (2019) [35] evaluated the performance of the EAARL and EAARL-B sensors in mapping various ranges of river sizes and concluded RMSE between 0.11 and 0.52 m where higher uncertainties were associated with the existence of turbulence (whitewater) and turbidity. Yoshida et al. (2022) [37] have evaluated the Lieca Chiroptera II sensor in mapping a river in Japan and reported 10 cm accuracy against ground surveys and RMSE of 8 cm, 10 cm, and 20 cm at the gravel bars, vegetated bed, and underwater bed, respectively. The performance of the Riegl VQ880-G sensor has been evaluated in the studies of Mandlburger et al. (2015) [21] and Miller

and Addy (2019) [39] and showed smaller bands of uncertainties (<0.10 m) and higher mapping resolutions (>20 points/m^2) than the Aquarius and the EAARL sensors. For the drone-based bathymetric LiDAR sensors, the performance of the Riegl VQ840-G has been evaluated in the study of Mandlburger et al. (2020) [30] and showed a close performance to the Riegl VQ880-G. The performance of the ASRTALiTe EDGE sensor has been evaluated in the study of Kinzel et al. (2021) [40] in the light of stream optical properties and suspended sediment concentration against RTK and MBES measurements. The study reported that the correspondence of LiDAR depths R^2 varies between 0.60 to 0.97 against the RTK measurements and 0.72 against the MBES measurements. Moreover, the study shows that the sensor maps deeper in gravel-bedded rivers where suspended sediment concentration is less than in sand-bedded rivers. The study of Islam et al. (2022) [41] investigated the effect of seasonality on the mapping quality of the TDOT GREEN sensor. The study found that the LiDAR measurements produce higher errors (RMSE) in autumn measurements when higher suspended sediment concentration exists than in the winter season.

Given the different specifications of the available bathymetric LiDAR sensors [42] and the various potential sources of uncertainties, a quantitative comparison study of different sensors applied in similar conditions may demonstrate differences in performance that helps in future applications and management use. However, to the authors' knowledge, no comparative studies have been conducted in that respect in a river environment. In this study, we present a comparative study of three different bathymetric LiDAR sensors, applied in a steep Norwegian river, and used with different acquisition approaches. The main objective is to conduct a quantitative assessment of their performances in mapping the river bathymetry under different morphological conditions and different acquisition approaches. We compare the river bathymetry (the elevation of the river bottom) derived from the bathymetric LiDAR sensors CZMIL Supernova, Riegl VQ880-G, and Riegl VQ840-G against bathymetry data from a multibeam echosounder (MBES) (Norbit Winghead i77h) and a terrestrial laser scanner (TLS) (Leica ScanStation P50) in pre-defined sub reaches of the river Lærdal in Norway. Both a comparison of point clouds from the instruments and a comparison of digital elevation models created from the point clouds were carried out. Three main objectives have been defined for the current study:

1. Evaluate the differences in elevation between the bathymetric LiDAR point clouds and the MBES and TLS point clouds.
2. Evaluate the differences in elevation of the bathymetric LiDAR point clouds against each other.
3. Relating the differences to river features such as depth, steepness of banks, abrupt elevation changes, and whitewater locations.

2. Data

2.1. Study Site

Lærdal River is located in a steep mountainside valley in Sogn og Fjordane County at the west of Norway. The study reach (stretches for 15 km), shown in Figure 1, drains a mountainous catchment of 994 km^2 with an unregulated daily mean discharge of around 31 m^3/s. The average width of the river ranges between 50 and 70 m linking flat banks of around 2.2 degrees of slope [22]. The longitudinal slope of the river is around 0.43 percent [22]. The dominant flood regime in the river is spring flood driven by rain events over snow melting events [43], and 72% percent of the adjacent areas are protected against those floods through embankments [22]. A series of weirs have been built along the river partly to compensate for the changes in the water-covered area due to the hydropower regulation of the river, and partly for improving recreational fishing for Atlantic salmon [44]. A survey was carried out for the reach from the Kuvelda tributary to the ocean (approximately the last two-thirds of the study reach) by Skår et al. (2017) [45] and found that around 67% of the reach had smooth-flowing conditions, while 32% and 1% were rapid and whitewater conditions, respectively. The study also found that the stretch was largely dominated by cobbles (51% coverage of the total area). Gravel composed 25% of the remaining substrate,

and boulders generally found along the riverbank and at the weir crests constitute 12% of the substrate. To our knowledge, no measurements for the water clarity, such as nephelometric turbidity units (NTU), were conducted for Lærdal, however, the visibility of the bottom is very good indicating clear water.
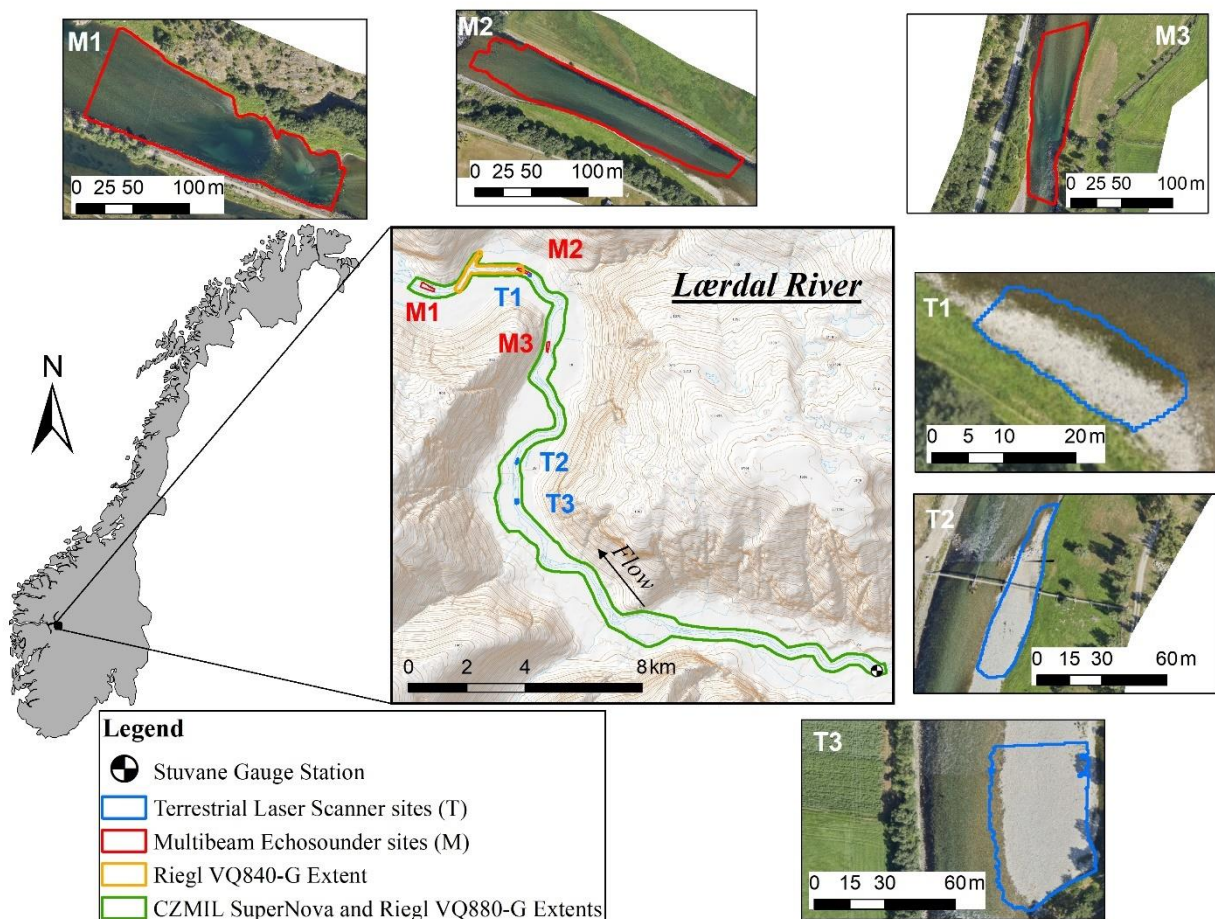

Figure 1. The study site location in Norway with the extent of the bathymetric LiDAR sensors, MBES, and TLS datasets. M and T denote the MBES and TLS datasets' locations, respectively. The spatial coordinate system is WGS 84/UTM zone 32N.

2.2. Bathymetric LiDAR Data

The river bathymetry of Lærdal was mapped in the fall of 2021 by three different bathymetric LiDAR sensors, CZMIL Supernova (fixed-wing aircraft), Riegl VQ880-G (fixed-wing aircraft) and Riegl VQ840-G (helicopter) (Table 1). The CZMIL and Riegl VQ880-G were applied for a continuous river mapping of the selected 15 km study reach whereas the Riegl VQ840-G was applied for a selected sub-reach in the study area (see Figure 1). The datasets were acquired and processed in accordance with the protocol "Production of Basis Geodata" [46] and delivered according to the requirements stated in the specification FKB-Laser v3.0 [47]. The procurement of the data allowed for 2% of misclassification in the delivered cloud. In general, the horizontal and vertical accuracies for all datasets were within 0.30 m and 0.10 m, respectively, achieved by utilising a set of 2 × 2 m control ground points (GCP) measured using RTK GNSS. The CZMIL and the Riegl VQ840-G datasets were acquired through regular patterns of crosslines with internally adjusting the strips before they adjusted to the GCPs. Although being a deep bathy (3 Secchi Depth) system, the CZMIL was operated in Shallow Bathy Mode for the Lærdal survey, therefore, the analysis is thus not evaluating the sensor running in deep mode. The Riegl VQ880-G dataset, on the other hand, was collected using a different acquisition pattern than the traditional

approach where the strip adjustment is performed together with the GCPs measured on the ground [48]. Figure 2 shows the different acquisition patterns followed in the bathymetric LiDAR collection.

Table 1. The specifications of the bathymetric LiDAR surveys.

	CZMIL Supernova	Riegl VQ880-G	Riegl VQ840-G
Sensor short name	CZMIL	VQ880	VQ840
Sensor type	Topo-Shallow Bathy [(1)]	Topo-Bathy	Topo-Bathy
Weight (kg)	270	65	12
Dimensions (cm)	89 × 60 × 90—sensor head 59 × 56.5 × 106—operation rack	52 × 52 × 69	36 × 29 × 20
Laser Channels (nm)	532/532/1064	532	532
Camera	Phase One iXM-RS150F	RGB	RGB
Measurement rate (kHz)	180	up to 550 kHz	50–200
Pulse Energy (mJ)	1.75	-	-
Pulse Duration (ns)	1.57	1.5	1.5
Field of view (deg)	±20	±20	±20
Beam divergence (mrad)	1.9	0.7–1.1	1–6
Input optics diameter (mm)	200		
Nominal flying altitude (m)	400–600	400	50–150
Laser footprint (cm)	75–112	50 @ 1.1mrad	5 to 90
Scan pattern	circular	circular	elliptical
Depth performance @ 15% Bottom Reflectance (Secchi depth)	2	1.5	2
Acquisition Date	21 July 2021	26 September 2021	25 September 2021
Discharge (m³/s)	20	15	15
Flight Height (m AGL)	~400	~400	~95
Laser footprint (cm)	75	40	21
Flight Lines excluding turns (km)	45.3	332.3	9.1
Coverage Topo-Bathy (km²)	3.6	3.6	0.2
Efficiency Topo-Bathy (km / km²)	12.7	93.2	54.8
Requested Density Bathy (point/m²)	5	5	5
Actual Density Bathy (point/m²)	6	91	40

[(1)] The CZMIL sensor was operated in shallow bathy mode only.
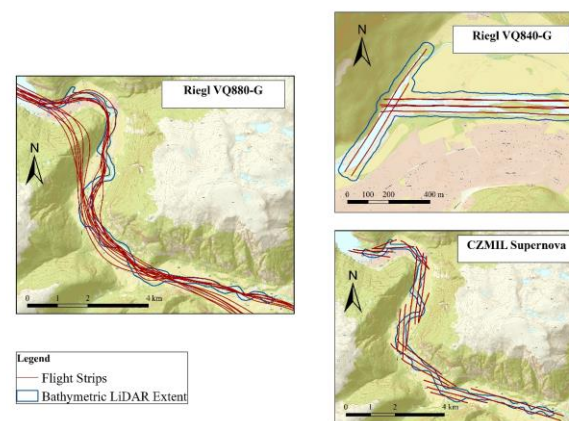

Figure 2. The acquisition patterns for the three bathymetric LiDAR datasets.

2.3. MBES and TLS Datasets

To evaluate the performance of the three bathymetric LiDAR sensors, we compared the river bottom (z level) measurements of the sensors against two sets of validation dataset, bathymetric data using Norbit Winghead i77h with integrated Applanix PosMV Oceanmaster [49,50] and terrestrial data at gravel bars using Leica ScanStation P50 laser scanner [51]. MBES data were collected on the 18th of November 2021 on a discharge of 20 m³/s during the measurements. TLS data were collected on the 25th and 26th of March

2022 and the corresponding discharges were 19 and 20 m^3/s, respectively. The locations of the MBES and the TLS sites are shown in Figure 1.

The MBES dataset was collected at three sites (M1–3) located in the lower 500 m of Lærdal river (Figures 1 and A1). M1 is located near the river outlet, with an average depth of two meters. The site includes a submerged boulder weir with a downstream pool of 10 m depth and protected riverbanks with pitched boulders. M2 is located upstream of a weir with an average and maximum water depth of 1.4 and 2.8 m, respectively. The flow pattern at the site could be described as a calm pool with uniformly gravel sediments and one side protected bank. M3 has an average and maximum water depth of 1.5 and 4.7 m, respectively, and contains scattered large boulders near the middle of the right bank, possibly remaining bank protections. The MBES dataset was acquired according to the Norwegian Mapping Authority Hydrography standards [46]. At the maximum water depth of 10 m (Figure A1), the absolute horizontal accuracy of data acquired by MBES was ±0.66 m, the absolute vertical accuracy was ±0.14 m, and the absolute water depth precision was ±0.10 m.

For the TLS datasets, the three sites consisted of uniform gravel sediments free of vegetation. At the T2 site, a pile of boulders exists of an old dry weir at the downstream right side. The TLS dataset was acquired with a bundle error below 8 mm, a cloud-to-cloud error up to 1.1 cm, and a maximum target error of 6 mm. Absolute positioning for both MBES and TLS was achieved using the Norwegian Mapping Authority CPOS RTK network.

3. Methodology

The performance of the three bathymetric LiDAR sensors was evaluated by comparing classified LiDAR and MBES point clouds, for the underwater geometry, and LiDAR and TLS point clouds, for the dry geometry. The evaluation of the point clouds was limited to the points classified as bare ground and water bathymetry. The differences (residuals) between the two point clouds were calculated as follows:

$$\text{residual}(i) = Z_f(i) - Z_b(i) \tag{1}$$

where $Z_f(i)$ denotes the MBES or TLS bed elevation and $Z_b(i)$ denotes the bathymetric LiDAR sensor bed elevation at the location i. Therefore, positive residual indicates that the bed elevation measured by the MBES or the TLS instruments is higher than the bathymetric LiDAR sensor bed elevation, and therefore the bathymetric LiDAR sensor overestimates the depth of the water. Conversely, negative residual indicates that the bed elevation of the MBES or the TLS instruments is lower than the bathymetric LiDAR sensor bed elevation, and hence the bathymetric LiDAR sensor underestimates the depth.

The residuals between the point clouds of the three bathymetric LiDAR were calculated following the same approach as in Equation (1). For the comparison of the Riegl VQ880-G against the CZMIL, positive residual indicates the bed elevation of the Riegl VQ880-G is higher than the CZMIL elevation, and therefore the CZMIL mapped deeper. For the comparison of the Riegl VQ840-G against the Riegl VQ880-G, positive residual indicates the Riegl VQ880-G mapped deeper, and for comparison of the Riegl VQ840-G against the CZMIL, positive residuals indicate that the CZMIL mapped deeper.

The residuals were calculated in two forms, cloud to cloud approach and raster to raster approach. For the point cloud approach, the Multiscale Model to Model Cloud Comparison method (M3C2) implemented in the CloudCompare Software (version 2.11.3) was used to estimate the residuals between the point clouds [52,53]. This method uses the 3D point cloud in estimating the distance between two clouds. The method is known for its advantages in eliminating meshing uncertainties and its robustness to missing data in comparing clouds with different roughness. The normal scale (D) and the projection scale (d) for the M3C2 were optimized based on the cloud with the least point density from the available datasets, following the recommendation criteria of Lague et al. (2013) [53]. The normal scale was set to 5 m, and the projection scale was set to 3 m, and both were found to be satisfactory for the analysis. Tests for the sensitivity of the overall results against

the selected scales were carried out and found the differences to be negligible. For the raster-based comparison, the digital elevation model of difference (DoD) is a common method in studying the sediment budget over a period of time (e.g., [21,54–57]). In this study, a 0.5 m cell size of raster was created using GDAL python package and the mean elevation of the points lying within the raster was assigned as the elevation of the cell.

The spatial distribution, the median, and the root mean squares (RMS) of the resulting residuals from the comparison approaches were examined as well as the frequency distributions of the residuals. To further investigate the characteristics of frequency distributions of the residuals, the skewness and kurtosis, were computed. Within the LiDAR applications, higher-order moment statistics (skewness and kurtosis) are usually used for filtering and classification of the LiDAR point cloud to classify the different objects (e.g., [58,59]). The mathematical expression for the skewness and the kurtosis can be summarized as follows [59]:

$$M^{(n)} = \left(\frac{1}{N\sigma^n} \sum_{i=1}^{N} (x_i - \mu)^n \right)^{\frac{1}{n}} \tag{2}$$

where $n = 3$ for skewness and $n = 4$ for kurtosis, respectively; N is the number of points; x_i is the residual of the ith point; μ and σ^2 are the mean value and the variance of the residual population. The skewness measures the asymmetry of a population. A zero skewness indicates a symmetrical distribution, negative skewness indicates a left-tailed distribution, and positive skewness indicates a right-tailed distribution. The kurtosis is a measure of whether a distribution is heavy-tailed or light-tailed relative to a normal distribution (a kurtosis of 3). A larger kurtosis than 3 indicates a thin pointed distribution compared to normal distribution while smaller kurtosis than 3 indicates broad flat distribution compared to normal distribution.

Based on the linear error propagation of the expected vertical accuracy of the bathymetric LiDAR sensors, the MBES, and the TLS, acceptance limits of the residuals for the comparison scenarios were specified. For the comparison of the bathymetric LiDAR sensors against the MBES, the acceptance limit of the residuals was set to ±0.20 m. For the comparison of the bathymetric LiDAR sensors against the TLS, since the vertical accuracy of the TLS is very small compared to the bathymetric LiDAR accuracy, the acceptance limit was fixed to the accuracy of the bathymetric LiDAR sensors, and hence ±0.10 m. For the comparison of the bathymetric LiDAR sensors against each other, the accuracy of each of the two sensors was included and therefore set to ±0.20 m. The percentage of the point cloud with residuals within the acceptance limits was computed and reported as the acceptance percentage.

Finally, an evaluation of the locations of residuals higher than the acceptance limits was carried out and analysed. The high residual locations were investigated with respect to the water depth, the slope of the river banks, abrupt elevation change locations, and the whitewater locations.

4. Results

Correspondence between the bathymetric LiDAR sensors' elevations and the MBES and the bathymetric LiDAR sensors' elevations and the TLS instruments' elevations are summarized in Figures 3 and 4. In general, the correspondences of the sensors with both instruments show high coefficients of determination (R^2) being greater than 0.9 in all cases. The correspondence against the MBES shows a general trend of all the LiDAR sensors' elevation to deviate from the MBES elevations by the same degree at higher elevations (upper right in Figure 3). Moreover, the Riegl VQ880 sensor showed some outliers at the M1 site (Figure 3a) at the lowest elevations from the MBES measurements that did not occur with the CZMIL sensor. This difference was not observed at any of the other MBES sites. The correspondence of the sensors to the TLS measurements shows similar high R^2 coefficients (greater than 0.9) as seen in Figure 4. The CZMIL showed a consistent fluctuation trend at all TLS sites of underestimation of the TLS elevations at the lower

elevations and overestimation at the higher elevations. The Riegl VQ880 sensor showed some high deviations from the TLS elevations at T3 site (Figure 4c).
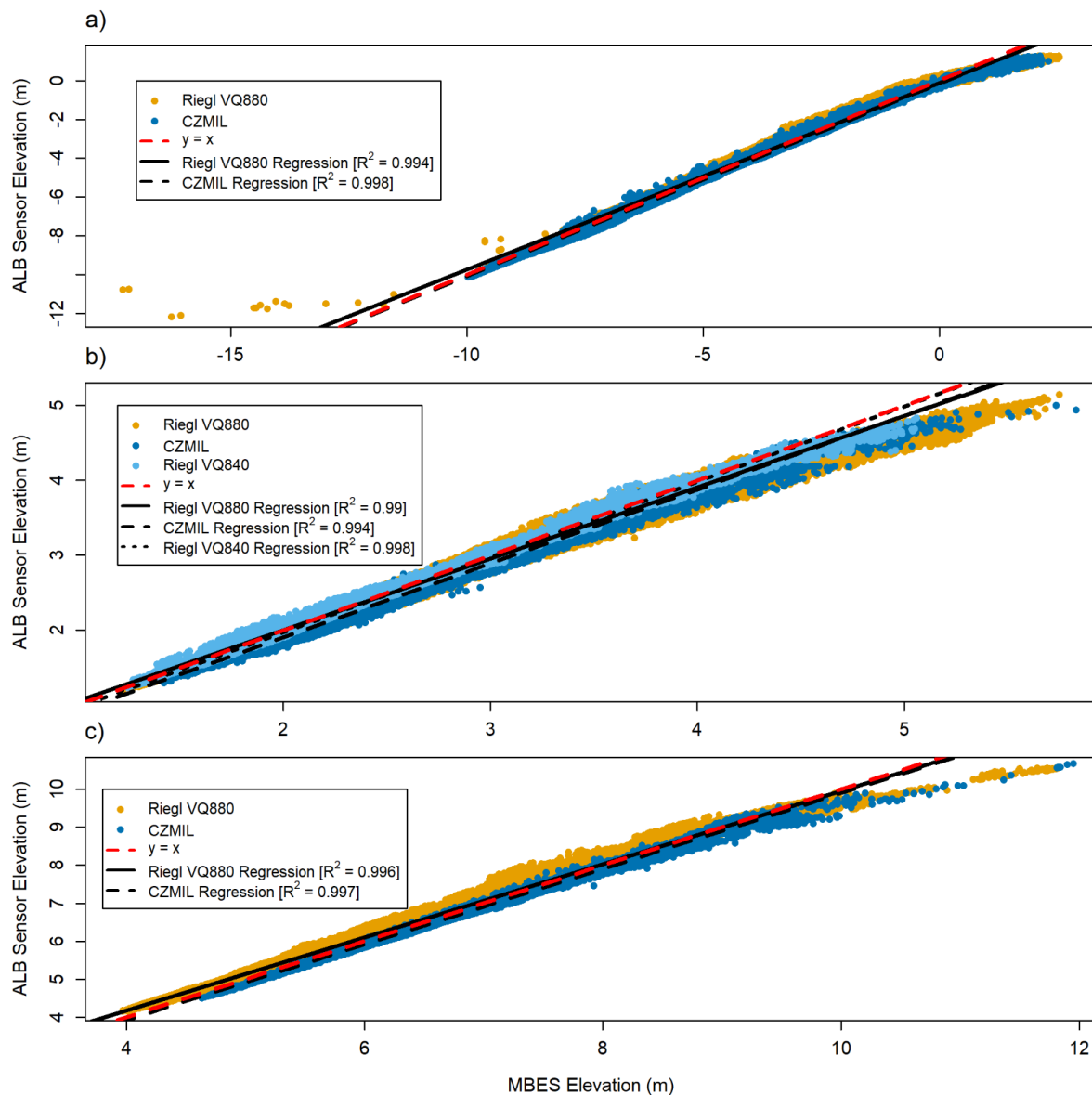

Figure 3. The correspondence between the MBES and the bathymetric LiDAR sensor elevations for the three MBES locations M1 (**a**), M2 (**b**), and M3 (**c**).

An illustration of the spatial distribution of the residuals from the comparison of the bathymetric LiDAR sensors against the MBES and the TLS is shown in Figures 5 and 6. For the comparison against the MBES, the residuals showed to be consistent within the riverbed region and increased near the banks and at the top of the weir crest at the M1 site (Figure 5). The Riegl VQ880-G sensor generally reported overall shallower elevations than the MBES measurements at M1 and M2 (negative M3C2 residuals) and deeper elevations than the MBES at M3, while the CZMIL sensor showed consistent shallower elevations than the MBES data at all the sites. The small intersection of the Riegl VQ840-G with the MBES dataset at M2 showed overall shallower elevations. For comparison against the TLS dataset (Figure 6), the CZMIL sensor showed a systematic residual variation closer to the wetted area while the Riegl VQ880-G residuals showed to be distributed randomly.
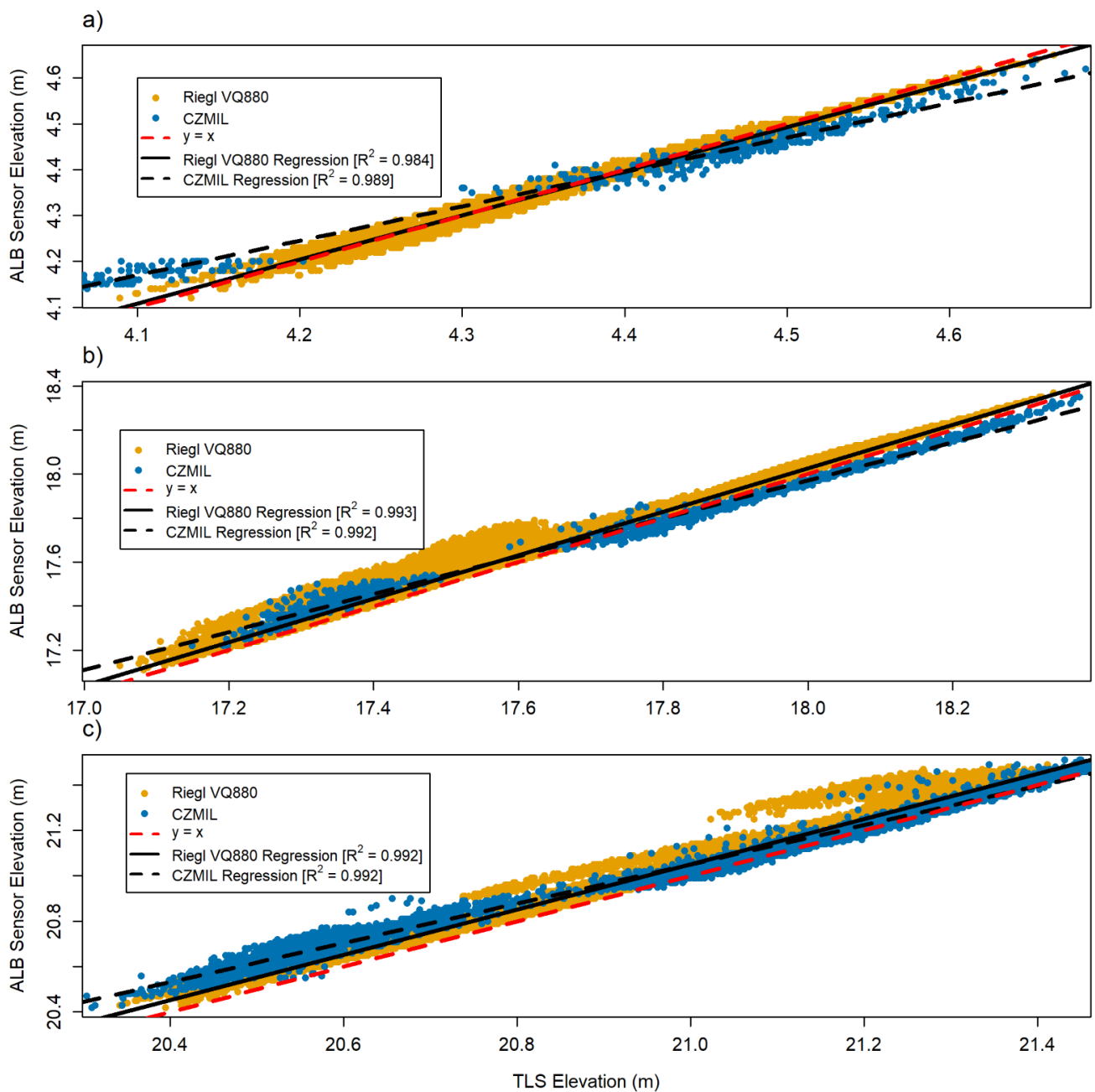
Figure 4. The correspondence between the TLS and the bathymetric LiDAR sensor elevations for the three TLS locations T1 (**a**), T2 (**b**), and T3 (**c**).

A summary of the median and the root mean square (RMS) of the residuals and the percentage of the accepted point cloud are shown in Table 2. The median of residuals showed to be consistent with the trends of their spatial distributions (Figures 5 and 6). The comparison against the MBES showed maximum median of 8 cm for the Riegl VQ880-G, 13 cm for the CZMIL, and 3 cm for the Riegl VQ840, where the maximums showed to be at M1 site. The minimum acceptance percentage of the point cloud, on the other hand, that showed residuals within 20 cm variations in the comparison against the MBES was 94% for all the sensors. The maximum RMS of the residuals in the point approach was 0.15 m, while almost double of that was found in the raster comparison.
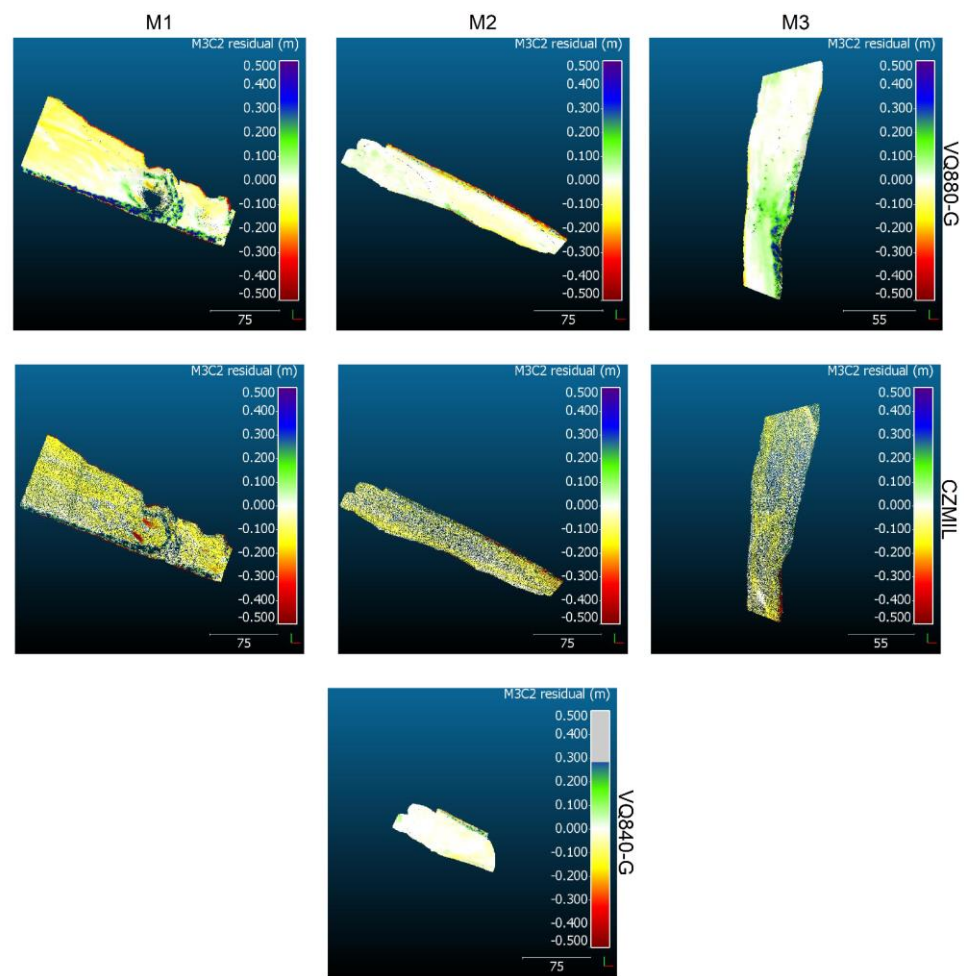
Figure 5. Residual (M3C2) maps for the bathymetric LiDAR sensors comparison against the MBES from CloudCompare Software. The colour saturation is limited to ±0.5 m residual. For illustration purposes, the sizes of the points were increased and adjusted.
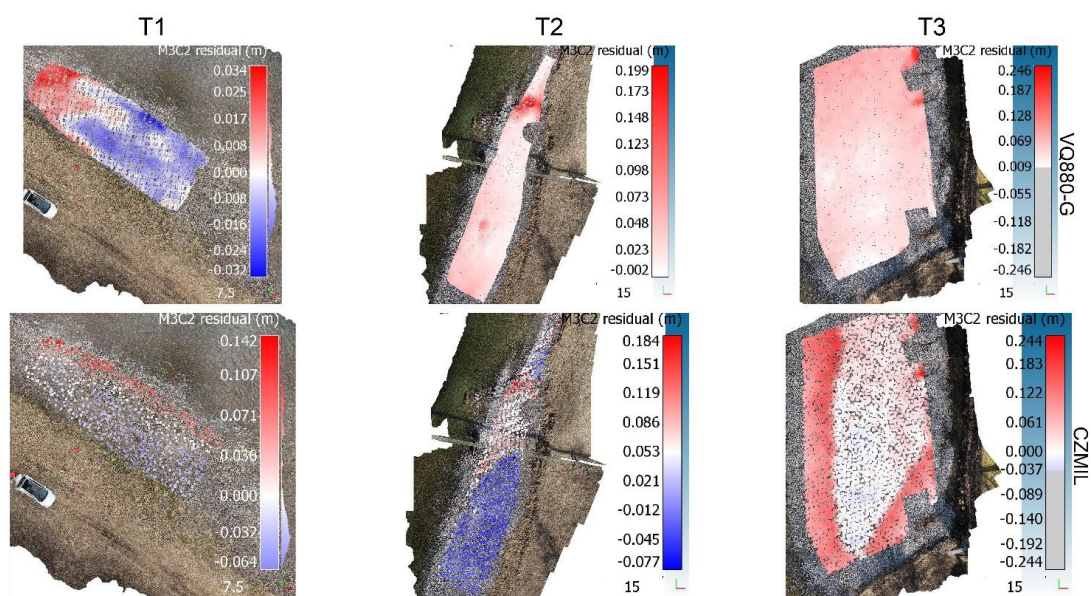

Figure 6. Residual (M3C2) maps for the bathymetric LiDAR sensors comparison against the TLS from CloudCompare Software. The sizes of the cloud points were adjusted for the purpose of the illustration. The background drone aerial photo was collected during the TLS measurements.

Table 2. The median residual and the maximum root mean square of the residuals, in meters, for point and raster approaches together with the acceptance limit of the residuals and the percentage of the accepted point cloud for the comparison of the bathymetric LiDAR sensors against the MBES (M1–3), the TLS (T1–3), and against the sensors each other.

	Location	Comparison Scenario	Median [1]		RMS		Acceptance Percentage [2]	Acceptance Limit
			DEM	M3C2	DEM	M3C2		
MBES *vs.* *ALB*	*M1*	MBES vs. Riegl VQ880	−0.07	−0.08	0.23	0.12	96	
		MBES vs. CZMIL	−0.13	−0.13	0.22	0.15	94	
		MBES vs. Riegl VQ840 [3]	NA	NA	NA	NA	NA	
	M2	MBES vs. Riegl VQ880	−0.05	−0.03	0.11	0.08	97	±0.20
		MBES vs. CZMIL	−0.11	−0.11	0.15	0.12	96	
		MBES vs. Riegl VQ840 [4]	−0.03	−0.03	0.09	0.03	100	
	M3	MBES vs. Riegl VQ880	0.04	0.04	0.11	0.06	99	
		MBES vs. CZMIL	−0.09	−0.09	0.14	0.11	99	
		MBES vs. Riegl VQ840 [3]	NA	NA	NA	NA	NA	
TLS *vs.* *ALB*	*T1*	TLS vs. Riegl VQ880	0.00	−0.01	0.02	0.01	100	
		TLS vs. CZMIL	−0.02	−0.02	0.06	0.05	94	
	T2	TLS vs. Riegl VQ880	0.03	0.03	0.04	0.04	98	±0.10
		TLS vs. CZMIL	−0.02	−0.02	0.06	0.05	96	
	T3	TLS vs. Riegl VQ880	0.04	0.05	0.05	0.06	99	
		TLS vs. CZMIL	0.04	0.04	0.08	0.08	71	
ALB *vs.* *ALB*	*Full Reach*	Riegl VQ880 vs. CZMIL	−0.10	−0.12	0.21	0.16	82	
	VQ840 Extent	Riegl VQ840 vs. Riegl VQ880	0.02	0.02	0.13	0.07	99	±0.20
	VQ840 Extent	Riegl VQ840 vs. CZMIL	0.13	0.12	0.27	0.22	82	

[1] Negative median residual in the comparison against the MBES and the TLS implies that the bathymetric LiDAR is the shallower while in the comparison of the bathymetric LiDAR against each other, the first in comparison scenario is the shallower. [2] The acceptance percentage is calculated based on the resulted residuals of the point approach from the acceptance limit. [3] No intersection between the MBES datasets and the Riegl VQ840-G sensor at these locations. [4] The corresponding values were calculated for the small intersection of the Riegl VQ840-G sensor with M2 (See Figure 3).

The comparison of the sensors against the TLS in the dry gravel bars indicated generally much smaller residual ranges compared to the MBES, with a maximum of 5 cm median residual encountered at T3. Moreover, due to the smaller ranges of residual compared to the MBES, the residual patterns of the comparison against the TLS did not show a clear trend of over/underestimation in comparison with the TLS elevation, especially with CZMIL at T1 and T2 sites. In addition, for the T3 site, although the median error is only 4 cm of overestimation, the associated outliers larger than 10 cm was 29% of the point cloud.

For the comparison of the bathymetric LiDAR sensors against each other, the comparison of the Riegl VQ880-G against CZMIL along the whole reach showed a deeper mapping of the Riegl over the CZMIL of around 10 to 12 cm median and 82% of the clouds were within 20 cm residuals. The comparison of the Riegl VQ840-G with the VQ880-G showed very small residuals of around 2 cm, while against the CZMIL, it showed a higher variation of around 13 cm where the CZMIL mapped deeper.

The frequency distributions of the residuals obtained from comparing bathymetric LiDAR against the MBES in point cloud and raster formats are shown in Figure 7. Overall, the residuals resemble single peak frequency distribution, and the two comparison approaches replicate similar residual distributions with minor differences across all MBES sites. Moreover, consistent with the general statistics in Table 2, the frequency distribution for Riegl VQ880-G showed the major frequencies in M1 and M2 sites to be shifted toward underestimation, while more toward overestimation in the M3 site, while for the CZMIL, the major frequencies indicate a consistent underestimation in all the sites, and the small intersection of M2 with the Riegl VQ840-G showed an overall underestimation in the frequency distribution.
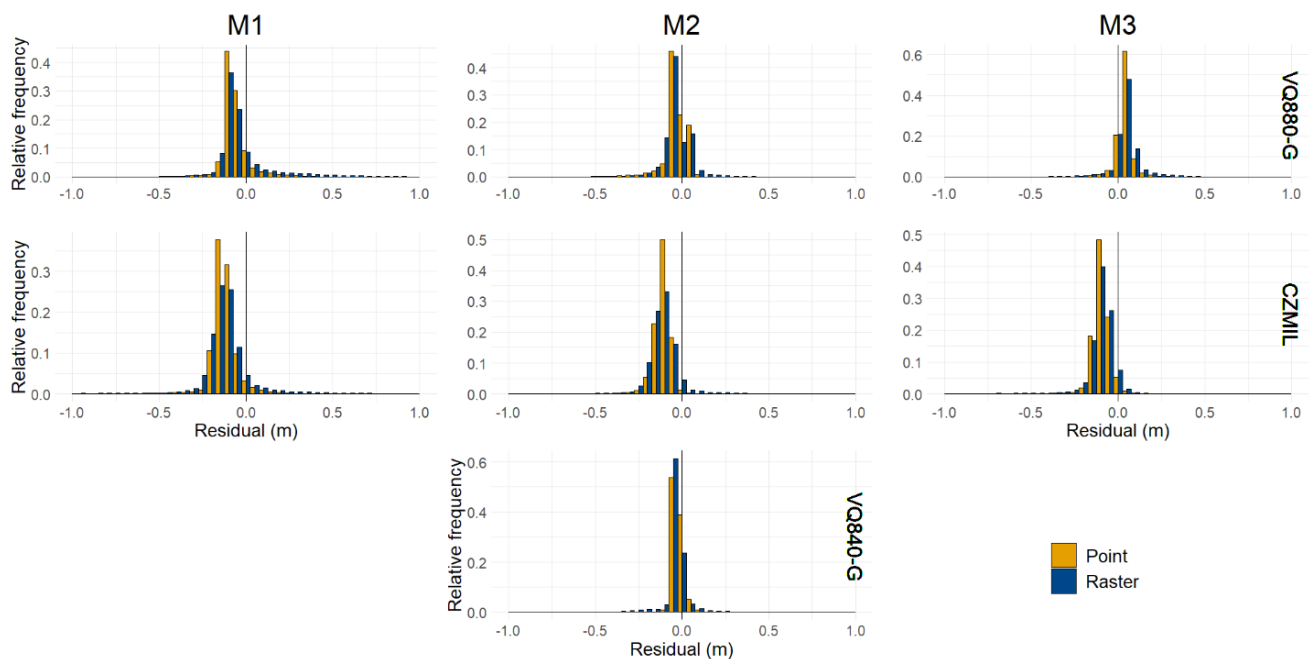
Figure 7. Frequency distributions of the residuals for the comparisons of the bathymetric LiDAR sensors against the MBES. The bin size for all histograms is 5 cm.

The frequency distributions of the residuals obtained by the comparison of the CZMIL and VQ880-G sensors against the TLS datasets are shown in Figure 8. The comparison against the VQ880-G sensor showed a single peak frequency distribution across all TLS sites, while the CZMIL showed a consistent double peak frequency distribution in T1 and T2, and T3 for the point comparison approach. The VQ880-G sensor showed a slight overestimation tendency for T2 and T3, while the double peak frequency distributions for the CZMIL make it difficult to draw similar conclusions from the distribution.
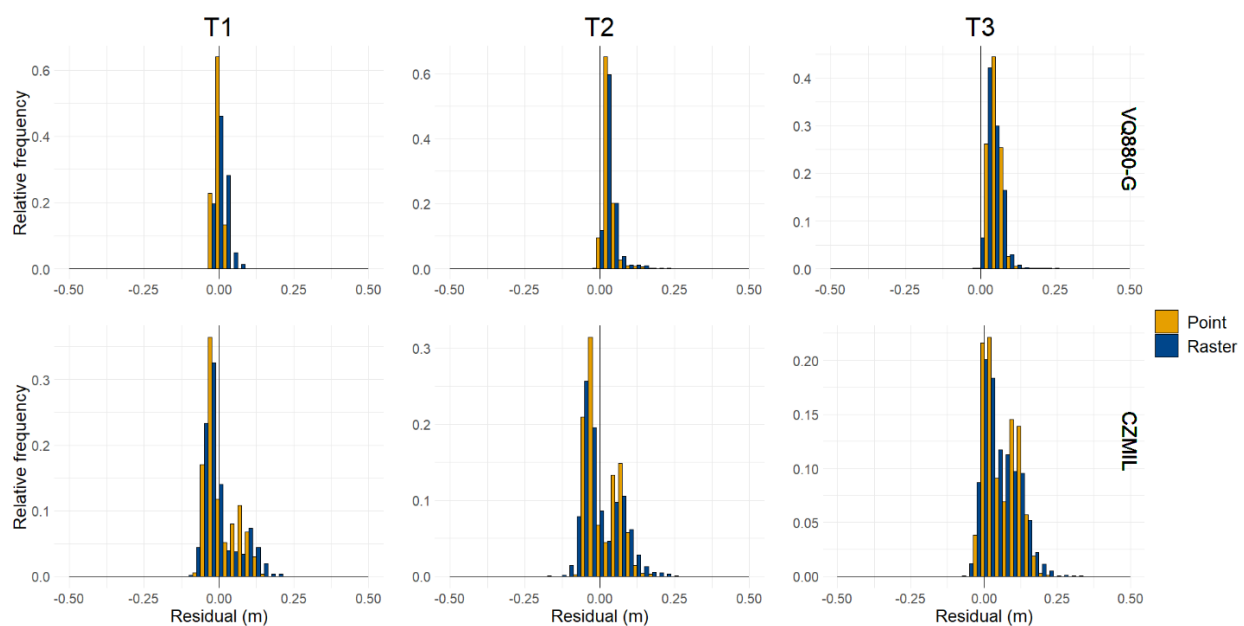

Figure 8. Frequency distributions of the residuals for the comparisons of the bathymetric LiDAR sensors against the TLS.

The frequency distributions of the residuals obtained by comparing the bathymetric LiDAR sensors against each other are shown in Figure 9. The comparison of the VQ880-G

against the CZMIL showed a clear tendency for the VQ880-G to map deeper in the two comparison approaches. For the two Riegl sensor comparisons, the frequency distribution resembles an almost symmetrical distribution around zero. For the CZMIL comparison against the VQ840, the frequency distribution shows a clear tendency of the CZMIL to map deeper.
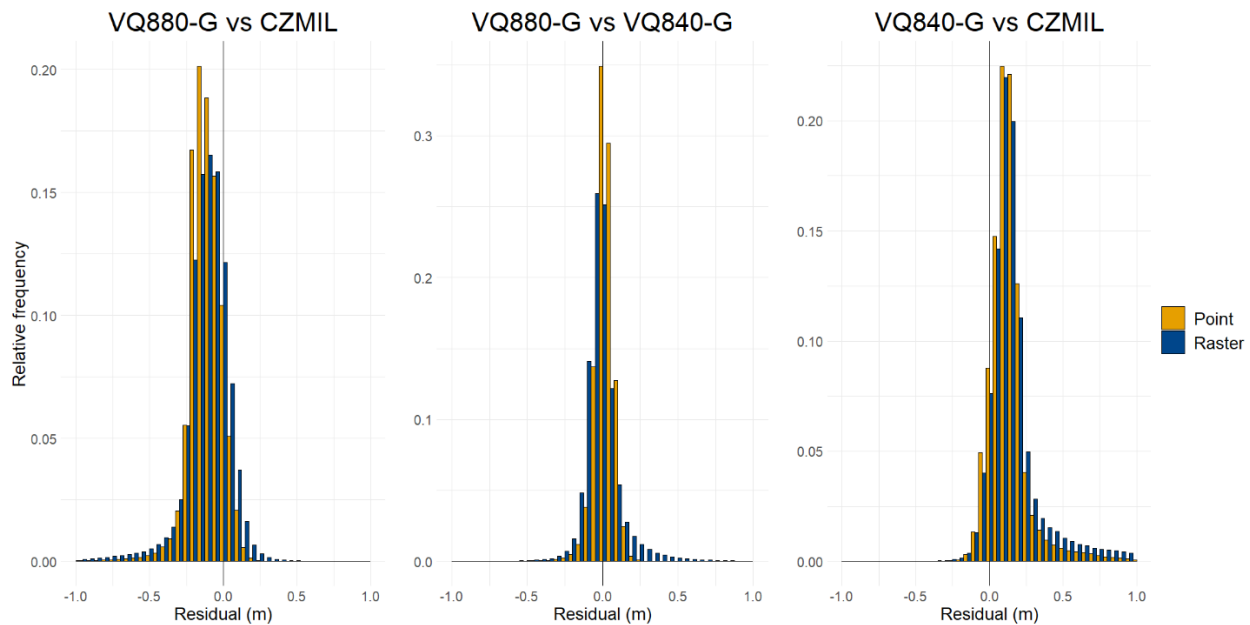

Figure 9. Frequency distributions of the residuals for the comparisons of the bathymetric LiDAR sensors against each other.

The mean, standard deviation, skewness, and kurtosis for the distributions of the residuals are summarized in Table 3. For all the comparison scenarios, the skewness results show asymmetrical distributions of the residual ranging from lightly skewed (less than ±0.5) to heavily skewed (larger than ±1.0) according to Bulmer (1979) [60]. The kurtosis statistics show peaked distributions of the residuals for both the comparison of liDAR sensors against the MBES measurement and in the intercomparison scenarios (kurtosis larger than 3). However, for the TLS comparison, the Riegl VQ880 sensor show peaked distributions, consistent with the other comparison scenarios, while the CZMIL sensor results in broad flat distributions compared to the normal distribution.

The analysis of the residual against the water depth for all the comparison scenarios shows no clear correlation between the residual magnitude and the depth. However, at the M1 site, the VQ880-G was not able to map depths of more than about 9 meters, while the CZMIL mapped the entire deep region. The relationship between the residual development and the change in the bed slope of the river is shown in Figure 10. The boxplot shows that the inner quartile of the residuals increases with the increase in bed slope and hence the average of the residual. The slope also includes the abrupt elevation changes that occur due to a sudden substrate change in the river reach (high substrate size variability). From the comparisons of the cross sections that have abrupt changes due to boulders, the VQ880 was found to detect the changes better than the CZMIL where the latter did not manage to capture the variability in the substrate, and therefore these areas showed high residuals between the two sensors.

Table 3. Statistics of the residuals, mean, standard deviation, skewness, and kurtosis for the comparison of the bathymetric LiDAR sensors against the MBES (M1–3), the TLS (T1–3), and against the sensors each other for the M3C2 approach.

	Location	Comparison Scenario	Mean	Standard Deviation	Skewness	Kurtosis
MBES vs. ALB	*M1*	MBES vs. Riegl VQ880	−0.06	0.10	1.01	67.82
		MBES vs. CZMIL	−0.12	0.09	−0.73	22.06
		MBES vs. Riegl VQ840 [1]	NA	NA	NA	NA
	M2	MBES vs. Riegl VQ880	−0.03	0.07	−2.67	15.54
		MBES vs. CZMIL	−0.11	0.05	−1.54	13.51
		MBES vs. Riegl VQ840 [2]	−0.02	0.03	1.28	13.98
	M3	MBES vs. Riegl VQ880	0.04	0.05	−0.34	29.51
		MBES vs. CZMIL	−0.09	0.05	−2.82	47.21
		MBES vs. Riegl VQ840 [1]	NA	NA	NA	NA
TLS vs. ALB	*T1*	TLS vs. Riegl VQ880	0.00	0.01	0.71	2.98
		TLS vs. CZMIL	0.01	0.05	0.80	2.30
	T2	TLS vs. Riegl VQ880	0.03	0.02	2.89	15.66
		TLS vs. CZMIL	0.01	0.05	0.60	2.07
	T3	TLS vs. Riegl VQ880	0.05	0.02	1.77	11.48
		TLS vs. CZMIL	0.06	0.05	0.39	1.94
ALB vs. ALB	*Full Reach*	Riegl VQ880 vs. CZMIL	−0.12	0.12	−2.53	47.52
	VQ840 Extent	Riegl VQ840 vs. Riegl VQ880	0.02	0.07	−2.61	68.78
	VQ840 Extent	Riegl VQ840 vs. CZMIL	0.14	0.17	4.01	114.13

[1] No intersection between the MBES datasets and the Riegl VQ840-G sensor at these locations. [2] The corresponding values were calculated for the small intersection of the Riegl VQ840-G sensor with M2 (See Figure 3).
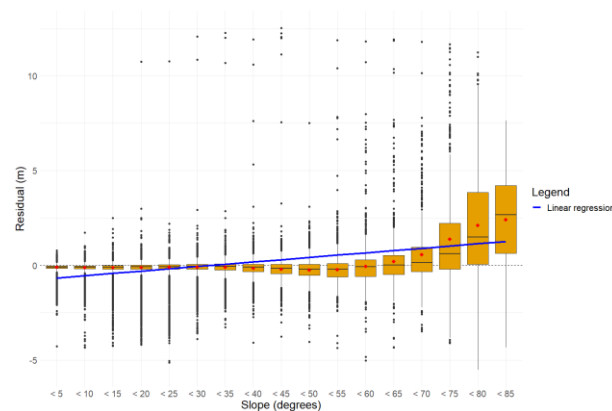

Figure 10. Boxplots for the residuals' development against the bathymetry's slope for the scenario of Riegl VQ880-G against CZMIL supernova in raster format. The blue line indicates a linear regression line of the average residual (red dots) at each slope category.

An illustration of the mapping abilities of the Riegl VQ880 and CZMIL sensors at whitewater locations is shown in Figure 11. Four sites where rapids and whitewater exist were selected. The comparison showed that the CZMIL seems to register points at the water surface as the bottom of the river, while the Riegl VQ880 seems less disturbed by the whitewater register deeper points.
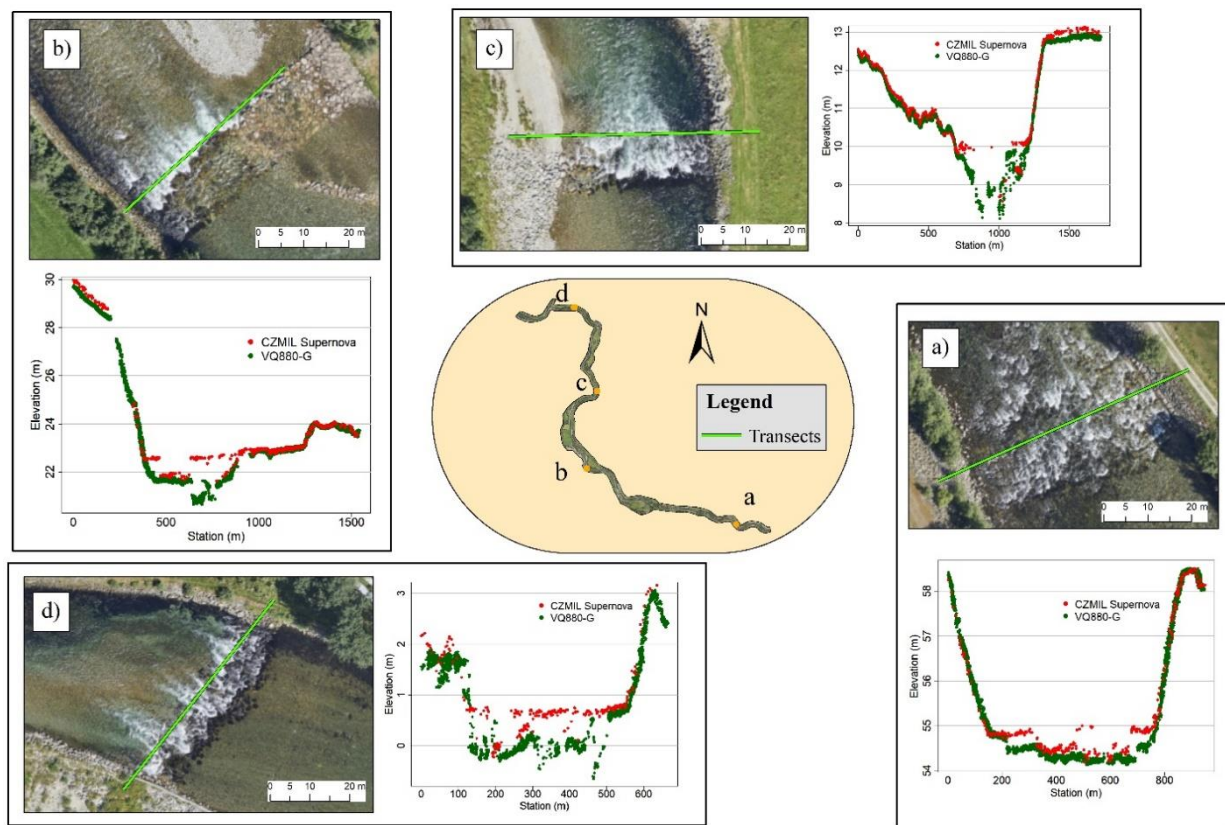
Figure 11. Cross-sectional illustration for the point cloud generated by the CZMIL and Riegl VQ880-G at whitewater locations. The aerial photo was obtained during the survey with CZMIL sensors.

5. Discussion

The development of bathymetric LiDAR technology has contributed significantly to both quality and quantity of river bathymetry data. In this study, we evaluated the performance of three different bathymetric LiDAR sensors, CZMIL Supernova, Riegl VQ880-G, and Riegl VQ840-G, used with different acquisition approaches, against MBES and TLS instruments in mapping bathymetry in the Lærdal river. Observed high residuals were evaluated with respect to their locations and examined against different river features such as water depth, bed slope, abrupt elevation changes, and locations of whitewater sections in the river.

The results show that all sensors perform well and produce high-quality bathymetry with the RMSE ranging from 2 to 23 cm compared to the MBES and the TLS instruments. Studies have examined the performance of the EAARL-B and Aquarius topobathymetric sensors in fluvial applications and have reported RMSE ranging between 11 to 52 cm [3,33,35,36]. Hilldale and Raff (2008) [13] evaluated the performance of SHOALS sensor, a system comparable to the CZMIL sensor, against data points collected with an RTK GPS and reported a median error between 14 to 27 cm using the raster comparison approach. In Lærdal, the range of the median error of the CZMIL sensor has shown to be between 0 and 13 cm against the MBES and the TLS (Table 2). The study of Mandlburger et al. (2015) [21] used the Riegl VQ880-G sensor to map the riverbed of the Pielach River with a median error of 1 cm. In Lærdal, the same sensor has shown median ranges between 3 to 8 cm against the MBES and 1 to 5 cm against the TLS, and since the accuracy values for Mandlburger et al. (2015) [21] is more representative for a smooth riverbed they compare to the residuals of the TLS comparison in Lærdal since the riverbed is composed of similar uniform gravels. The Riegl VQ840-G sensor was used in the study of Mandlburger et al. (2020) [30] and has shown an absolute accuracy of around 3 cm, and similar median residual has been found in the comparison of the same sensor against the MBES in Lærdal.

Moreover, the Riegl VQ840 sensor in Lærdal has shown similar RMSE to the TDOT GREEN sensor performance in the study of Islam et al. (2022) [41] where they reported around 7 cm RMSE for the underwater geometry (similar to the 9 cm for the Riegl VQ840 against the MBES). Therefore, in general, the performance of all the sensors lies within the accuracy ranges obtained in previous studies.

The difference in the residual range between the bathymetric LiDAR sensors compared with the MBES and the TLS has several potential explanations. First, the absolute horizontal and vertical accuracies for the MBES survey in Lærdal were ±0.66 m and ±0.14 m, respectively, and since most of the previous studies that have evaluated the performance of the bathymetric LiDAR sensors used more accurate validation sources (such as RTK measurements) [3,30,33,35,36], it is likely that part of the residuals of the bathymetric Li-DAR evaluation was introduced by the MBES system itself. This issue was also reported by Kinzel et al. (2021) [40] where they observed mismatches between the MBES measurements and the bathymetric LiDAR measurements due to the uncertainties of the GNSS positioning system deployed with the MBES. On the other hand, the TLS survey in Lærdal reported accuracies within ±0.01 m which is comparable to the accuracy of previous validation datasets used. Another potential reason is the difference in complexities between the MBES sites (M1–3) and the TLS sites (T1–3). The features of the bottom at the MBES locations are composed of variable grain sizes ranging from very fine sediments to large boulders varying abruptly at some locations, whereas the TLS sites are mostly gravel bars with uniform gravel sediments. For example, the M1 site has been shown to have the largest median residuals and RMS both for the CZMIL and the Riegl VQ880-G sensors (Table 2). The complexity of the site with the large, submerged weirs, the steep banks, the large boulders, and deep depths causes higher residuals compared to the other sites which are also encountered in the investigations of Kinzel et al. (2021) [40] and Islam et al. (2022) [41].

Despite the different CZMIL and Riegl VQ880-G acquisition approaches, the analysis shows that the acquisition patterns have little impact on the overall resulting residuals. In the MBES comparison, for example, The Riegl VQ880-G show variable overall residuals (underestimation at M1 and M2, and overestimation at M3) whereas the CZMIL has shown consistent underestimation across all the MBES sites (Figure 5). The tactical flying adopted in the Riegl VQ880-G mapping has allowed for maximising the illumination of the riverbed and better bottom detection. As a result, the strip adjustment technique needed for such kind of acquisition requires rigorous adjustment techniques that might lead to some challenges in the consistencies [48,61]. However, this has not affected the overall accuracy of the data.

The comparison of the residual's frequency distribution of the VQ880-G and the CZMIL sensors against the MBES and the TLS shows consistent single peak distributions for the VQ880-G sensor against the two instruments, while for the CZMIL sensors, it shows single peak distribution against the MBES and double peak distributions against the TLS (Figures 7 and 8). The CZMIL sensor is using two LiDAR sensors, a topo sensor with a wavelength of 1064 nm mainly used to map the dry terrain, and the other a bathy sensor with a wavelength of 532 nm (Table 1) to map sub-surface geometries. Additionally, since the topo sensor is likely to be more accurately calibrated against the GCPs, the part of the gravel bars scanned by the topo sensor showed to have fewer residuals (the peak closer to the zero in Figure 8) than the parts scanned by the topo-bathy sensors (the peak of the higher residuals in Figure 8). Moreover, the high kurtosis values for the frequency distributions of the residuals (Table 3) indicate that the share of the outliers (high residuals) is significantly less compared to normal distribution outliers, which supports the acceptance percentage reported in Table 2.

The comparison of the bathymetric LiDAR sensors against each other showed that since the two Riegl sensors share more or less similar characteristics with respect to the laser pulse strength and footprint size (Table 1), their comparison resulted in negligible deviations (Table 2 and Figure 9). On the other hand, the comparison of the CZMIL against the VQ840-G showed higher variations than against the VQ880-G (Table 2 and

Figure 9) since the characteristics of the CZMIL sensor are further from the VQ840-G than the VQ880-G (Table 1)

The analysis of the high residuals' relation to water depth has shown no clear correlation between residuals and water depths, similar to what has been reported by others [11,33,35]. However, since there is a deep pool at the M1 site where the depth exceeds 9 m, the low pulse strength sensor, the VQ880-G, misses that deep section, while the CZMIL sensor, a higher pulse strength sensor, captures that deep area very well. The point cloud resulting from the VQ880-G sensor started to shrink in terms of point density near 9 m, before totally missignaling at larger depths. The ASTRALiTe EDGE sensor in the study of Kinzel et al. (2021) [40] exhibited a similar issue with mapping depths higher than 9 m, and they suggested that this could be attributed to the extinction of the laser in deep water or due to unresolved positions from the river feature. The Riegl sensors, including the VQ840-G, share common characteristics with the ASTRALiTe sensor, and such performance seems to be common within the peer sensors.

The steep bank slopes and abrupt changes in bottom substrate size locations have shown high residuals, similar to what was reported by Kinzel et al. (2021) [40], Tonina et al. (2019) [35] and Hilldale and Raff (2008) [13]. The horizontal uncertainty, in such locations, can easily lead to high residuals since large elevation change occurs over short distances [13]. Across the different bathymetric LiDAR sensors, the footprint size parameter indicates the detailedness of the produced cloud where the smaller it is, the higher the sensor's ability to capture the details [3,35]. Therefore, in Lærdal's survey, since the footprint size of the two Riegl sensors is smaller than the CZMIL (Table 1), the Riegl is expected to capture the variation more accurately than the CZMIL.

Mapping whitewater locations has been a challenge for all LiDAR sensors [62]. This is also the case in Lærdal, where we particularly see less data in areas with riffles and outlets of weir basins. From the spatial distribution of the residuals between the CZMIL and the VQ880-G, large deviations have been observed between the sensors' clouds in these locations. Additionally, since no other measurements exists to compare the two clouds, a visual inspection of the cross-sectional geometries of the two clouds was employed for the evaluation (Figure 9). The illustration shows that the VQ880-G has produced a more realistic bottom profile, whereas the CZMIL was found to be more vulnerable to missing the river bottom at those locations and in some cases reported the water surface as the river bottom. The interference of the air entrainment with the laser pulse prevents the sensor from accurately measuring the bathymetry, and such an issue has been reported by Hilldale and Raff (2008) [13] from the SHOALS' evaluation. In addition, with a significantly higher point density produced from the Riegl VQ880-G flight pattern, the chance of accurately detecting the bottom in the whitewater section is higher than for the lower point density dataset from the CZMIL. This higher point density cloud could help the automatic classification algorithm to classify the bottom easier than what is the case in a low-density cloud from the CZMIL. Vegetation is also a common problem that challenges the autoclassification algorithms [62]. In Lærdal, high residuals have occurred on islands and in small streams covered with vegetation similar to what has been reported by Mandlburger et al. (2015) [21] and Tonina et al. (2019) [35]. Such areas will be associated with some level of uncertainties that one needs to be aware of when the LiDAR bathymetries are used.

To conclude, rivers are under pressure globally and the need to protect and restore riverine habitats is increasing. To achieve this, a detailed bathymetry of the rivers can form a basis for the analysis and modelling of impacts and restoration strategies. The bathymetric LiDAR sensors presented are capable of providing bathymetric data for rivers at an accuracy and level of detail that are beyond any other method we are currently deploying and could therefore provide highly important data for planning and creating detailed models. We, therefore, see this as a very useful method for providing the data needed for future work on river protection and restoration.

Appendix A

Example of the bathymetric map at the MBES sites (M1–M3) for the Riegl VQ880-G sensor and the corresponding water depth.
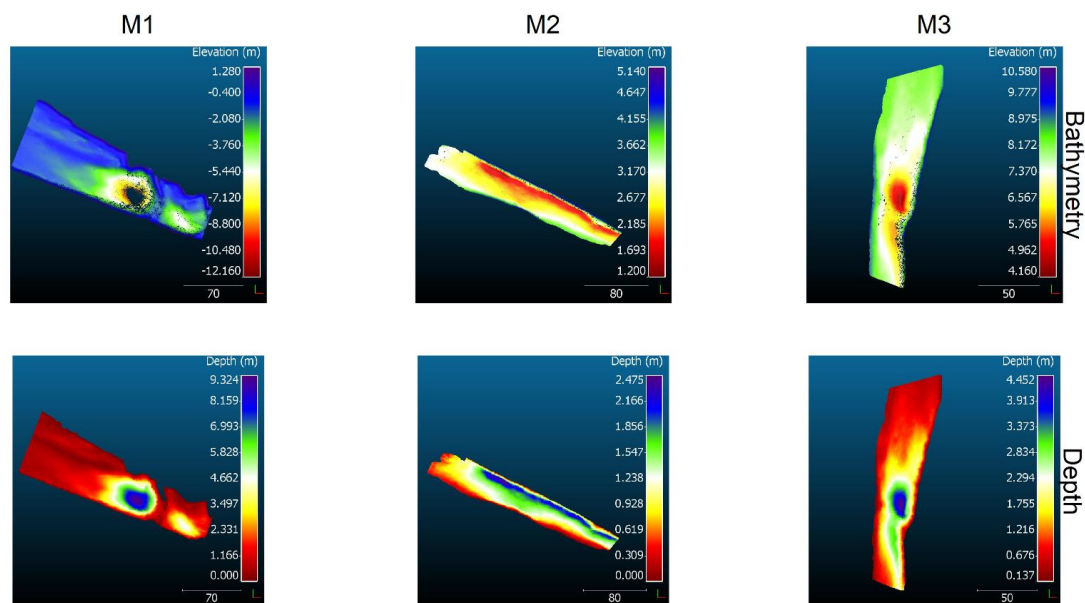

Figure A1. Bathymetric map at the MBES sites (M1–3) for the Riegl VQ880-G sensor and the corresponding water depth.

References

1. Saleh, F.; Ducharne, A.; Flipo, N.; Oudin, L.; Ledoux, E. Impact of river bed morphology on discharge and water levels simulated by a 1D Saint–Venant hydraulic model at regional scale. *J. Hydrol.* **2013**, *476*, 169–177. [CrossRef]
2. Cook, A.; Merwade, V. Effect of topographic data, geometric configuration and modeling approach on flood inundation mapping. *J. Hydrol.* **2009**, *377*, 131–142. [CrossRef]
3. Kinzel, P.J.; Legleiter, C.J.; Nelson, J.M. Mapping River Bathymetry with a Small Footprint Green LiDAR: Applications and Challenges. *J. Am. Water Resour. Assoc.* **2013**, *49*, 183–204. [CrossRef]
4. Winterbottom, S.J.; Gilvear, D.J. Quantification of channel bed morphology in gravel-bed rivers using airborne multispectral imagery and aerial photography. *Regul. Rivers Res. Manag.* **1997**, *13*, 489–499. [CrossRef]
5. Allouis, T.; Bailly, J.-S.; Pastol, Y.; Le Roux, C. Comparison of LiDAR waveform processing methods for very shallow water bathymetry using Raman, near-infrared and green signals. *Earth Surf. Process. Landf.* **2010**, *35*, 640–650. [CrossRef]
6. Bangen, S.G.; Wheaton, J.M.; Bouwes, N.; Bouwes, B.; Jordan, C. A methodological intercomparison of topographic survey techniques for characterizing wadeable streams and rivers. *Geomorphology* **2014**, *206*, 343–361. [CrossRef]

7. Hostache, R.; Matgen, P.; Giustarini, L.; Teferle, F.N.; Tailliez, C.; Iffly, J.-F.; Corato, G. A drifting GPS buoy for retrieving effective riverbed bathymetry. *J. Hydrol.* **2015**, *520*, 397–406. [CrossRef]
8. Dey, S.; Saksena, S.; Merwade, V. Assessing the effect of different bathymetric models on hydraulic simulation of rivers in data sparse regions. *J. Hydrol.* **2019**, *575*, 838–851. [CrossRef]
9. Casas, A.; Benito, G.; Thorndycraft, V.R.; Rico, M. The topographic data source of digital terrain models as a key element in the accuracy of hydraulic flood modelling. *Earth Surf. Process. Landf.* **2006**, *31*, 444–456. [CrossRef]
10. McKean, J.; Nagel, D.; Tonina, D.; Bailey, P.; Wright, C.W.; Bohn, C.; Nayegandhi, A. Remote Sensing of Channels and Riparian Zones with a Narrow-Beam Aquatic-Terrestrial LIDAR. *Remote Sens.* **2009**, *1*, 1065–1096. [CrossRef]
11. McKean, J.; Tonina, D.; Bohn, C.; Wright, C.W. Effects of bathymetric lidar errors on flow properties predicted with a multi-dimensional hydraulic model. *J. Geophys. Res. Earth Surf.* **2014**, *119*, 644–664. [CrossRef]
12. Gao, J. Bathymetric mapping by means of remote sensing: Methods, accuracy and limitations. *Prog. Phys. Geogr.* **2009**, *33*, 103–116. [CrossRef]
13. Hilldale, R.C.; Raff, D. Assessing the ability of airborne LiDAR to map river bathymetry. *Earth Surf. Process. Landf.* **2008**, *33*, 773–783. [CrossRef]
14. Legleiter, C.J.; Harrison, L.R. Remote Sensing of River Bathymetry: Evaluating a Range of Sensors, Platforms, and Algorithms on the Upper Sacramento River, California, USA. *Water Resour. Res.* **2019**, *55*, 2142–2169. [CrossRef]
15. Lefsky, M.A.; Cohen, W.B.; Parker, G.G.; Harding, D.J. Lidar remote sensing for ecosystem studies. *Bioscience* **2002**, *52*, 19–30. [CrossRef]
16. LaRocque, P.E.; West, G.R. Airborne Laser Hydrography: An Introduction. 1999. Available online: https://www.researchgate. net/profile/Paul-Larocque-2/publication/228867617_Airborne_laser_hydrography_an_introduction/links/544141ef0cf2e6f0 c0f607c0/Airborne-laser-hydrography-an-introduction.pdf (accessed on 15 June 2022).
17. Juárez, A.; Adeva-Bustos, A.; Alfredsen, K.; Dønnum, B.O. Performance of A Two-Dimensional Hydraulic Model for the Evaluation of Stranding Areas and Characterization of Rapid Fluctuations in Hydropeaking Rivers. *Water* **2019**, *11*, 201. [CrossRef]
18. Moniz, P.J.; Pasternack, G.B.; Massa, D.A.; Stearman, L.W.; Bratovich, P.M. Do rearing salmonids predictably occupy physical microhabitat? *J. Ecohydraulics* **2020**, *5*, 132–150. [CrossRef]
19. Saltveit, S.J.; Brabrand, Å.; Juárez, A.; Stickler, M.; Dønnum, B.O. The Impact of Hydropeaking on Juvenile Brown Trout (Salmo trutta) in a Norwegian Regulated River. *Sustainability* **2020**, *12*, 8670. [CrossRef]
20. Lague, D.; Feldmann, B. Chapter 2—Topo-bathymetric airborne LiDAR for fluvial-geomorphology analysis. In *Remote Sensing of Geomorphology*; Tarolli, P., Mudd, S.M., Eds.; Developments in Earth Surface Processes; Elsevier: Amsterdam, The Netherlands, 2020; Volume 23, pp. 25–54.
21. Mandlburger, G.; Hauer, C.; Wieser, M.; Pfeifer, N. Topo-Bathymetric LiDAR for Monitoring River Morphodynamics and Instream Habitats-A Case Study at the Pielach River. *Remote Sens.* **2015**, *7*, 6160–6195. [CrossRef]
22. Awadallah, M.O.M.; Juárez, A.; Alfredsen, K. Comparison between Topographic and Bathymetric LiDAR Terrain Models in Flood Inundation Estimations. *Remote Sens.* **2022**, *14*, 227. [CrossRef]
23. Juárez, A.; Alfredsen, K.; Stickler, M.; Adeva-Bustos, A.; Suárez, R.; Seguín-García, S.; Hansen, B. A Conflict between Traditional Flood Measures and Maintaining River Ecosystems? A Case Study Based upon the River Lærdal, Norway. *Water* **2021**, *13*, 1884. [CrossRef]
24. Quadros, N. Unlocking the characteristics of bathymetric LiDAR sensors. *LiDAR Magazine*, 3 December 2013; 62–67.
25. Feygels, V.; Ramnath, V.; Marthouse, R.; Aitken, J.; Smith, B.; Clark, N.; Renz, E.; Duong, H.; Wozencraft, J.; Reisser, J. CZMIL as a rapid environmental disaster response tool. In Proceedings of the OCEANS 2017—Aberdeen, Aberdeen, UK, 19–22 June 2017; 2017; Volume 2017, pp. 1–7.
26. Ramnath, V.; Feygels, V.; Kalluri, H.; Smith, B. CZMIL (Coastal Zone Mapping and Imaging Lidar) bathymetric performance in diverse littoral zones. In Proceedings of the OCEANS 2015—MTS/IEEE Washington, Washington, DC, USA, 19–22 October 2015. [CrossRef]
27. Wozencraft, J.M. Requirements for the Coastal Zone Mapping and Imaging Lidar (CZMIL). In Proceedings of the SPIE—The International Society for Optical Engineering, Orlando, FL, USA, 12 May 2010; Volume 7695.
28. Costa, B.M.; Battista, T.A.; Pittman, S.J. Comparative evaluation of airborne LiDAR and ship-based multibeam SoNAR bathymetry and intensity for mapping coral reef ecosystems. *Remote Sens. Environ.* **2009**, *113*, 1082–1100. [CrossRef]
29. Riegl Riegl VQ-880-NG data sheet. 2016. Available online: http://www.riegl.com/uploads/tx_pxpriegldownloads/RIEGL_VQ-880-G_Datasheet_2018-09-28.pdf (accessed on 15 June 2022).
30. Mandlburger, G.; Pfennigbauer, M.; Schwarz, R.; Flöry, S.; Nussbaumer, L. Concept and Performance Evaluation of a Novel. *Remote Sens.* **2020**, *12*, 28. [CrossRef]
31. Pfennigbauer, M.; Rieger, P.; Schwarz, R.; Ullrich, A. Impact of beam parameters on the performance of a topo-bathymetric lidar sensor. In Proceedings of the Laser Radar Technology and Applications XXVII, Orlando, FL, USA, 3 June 2022; Volume 12110, pp. 107–117. [CrossRef]
32. Wang, D.; Xing, S.; He, Y.; Yu, J.; Xu, Q.; Li, P. Evaluation of a New Lightweight UAV-Borne Topo-Bathymetric LiDAR for Shallow Water Bathymetry and Object Detection. *Sensors* **2022**, *22*, 1379. [CrossRef] [PubMed]

33. Fernandez-Diaz, J.C.; Glennie, C.L.; Carter, W.E.; Shrestha, R.L.; Sartori, M.P.; Singhania, A.; Legleiter, C.J.; Overstreet, B.T. Early Results of Simultaneous Terrain and Shallow Water Bathymetry Mapping Using a Single-Wavelength Airborne LiDAR Sensor. *IEEE J. Sel. Top. Appl. Earth Obs. Remote Sens.* **2014**, *7*, 623–635. [CrossRef]

34. Kinzel, P.J.; Wright, C.W.; Nelson, J.M.; Burman, A.R. Evaluation of an Experimental LiDAR for Surveying a Shallow, Braided, Sand-Bedded River. *J. Hydraul. Eng.* **2007**, *133*, 838–842. [CrossRef]

35. Tonina, D.; McKean, J.A.; Benjankar, R.M.; Wright, C.W.; Goode, J.R.; Chen, Q.; Reeder, W.J.; Carmichael, R.A.; Edmondson, M.R. Mapping river bathymetries: Evaluating topobathymetric LiDAR survey. *Earth Surf. Process. Landf.* **2019**, *44*, 507–520. [CrossRef]

36. Legleiter, C.J.; Overstreet, B.T.; Glennie, C.L.; Pan, Z.; Fernandez-Diaz, J.C.; Singhania, A. Evaluating the capabilities of the CASI hyperspectral imaging system and Aquarius bathymetric LiDAR for measuring channel morphology in two distinct river environments. *Earth Surf. Process. Landf.* **2016**, *41*, 344–363. [CrossRef]

37. Yoshida, K.; Maeno, S.; Ogawa, S.; Mano, K.; Nigo, S. Estimation of distributed flow resistance in vegetated rivers using airborne topo-bathymetric LiDAR and its application to risk management tasks for Asahi River flooding. *J. Flood Risk Manag.* **2020**, *13*, e12584. [CrossRef]

38. Yoshida, K.; Kajikawa, Y.; Nishiyama, S.; Islam, M.T.; Adachi, S.; Sakai, K. Three-dimensional numerical modelling of floods in river corridor with complex vegetation quantified using airborne LiDAR imagery. *J. Hydraul. Res.* **2022**, 1–21. [CrossRef]

39. Miller, P.; Addy, S. Topo-Bathymetric Lidar in Support of Hydromorphological Assessment, River Restoration and Flood Risk Management. *CREW Report*, 13 May 2019; 1–41.

40. Kinzel, P.J.; Legleiter, C.J.; Grams, P.E. Field evaluation of a compact, polarizing topo-bathymetric lidar across a range of river conditions. *River Res. Appl.* **2021**, *37*, 531–543. [CrossRef]

41. Islam, M.T.; Yoshida, K.; Nishiyama, S.; Sakai, K.; Tsuda, T. Characterizing vegetated rivers using novel unmanned aerial vehicle-borne topo-bathymetric green lidar: Seasonal applications and challenges. *River Res. Appl.* **2022**, *38*, 44–58. [CrossRef]

42. Mandlburger, G. A review of airborne laser bathymetry for mapping of inland and coastal waters. *Hydrogr. Nachr.* **2020**, 6–15. [CrossRef]

43. Gottschalk, L.; Jensen, L.J.; Lundquist, D.; Solantie, R.; Tollan, A. Hydrologic regions in the Nordic countries. *Nord. Hydrol.* **1979**, *10*, 273–286. [CrossRef]

44. Alfredsen, K.; Awadallah, M.O.M. *Vurdering av Hydraulisk Effekt av Tersklar i Lærdalselva*; NTNU: Trondheim, Norway, 2022.

45. Skår, B.; Gabrielsen, S.E.; Stranzl, S. *Habitatkartlegging av Lærdalselva fra Voll bru til sjø Laboratorium for Ferskvannsøkologi og Innlandsfiske*; NORCE: Bergen, Norway, 2017.

46. Statens Kartverk. Produksjon av Basis Geodata—Standarder Geografisk Informasjon. Version 1.0. 2015, pp. 1–94. Available online: https://www.kartverket.no/globalassets/geodataarbeid/standardisering/standarder/standarder-geografisk-informasjon/produksjon-av-basis-geodata-1.0-standarder-geografisk-informasjon.pdf (accessed on 15 June 2022).

47. Kartverket. Produktspesifikasjon Nasjonal Modell for Høydedata fra Laserskanning (FKB-Laser). No. Version 2.0, Norwegian Mapping Authorities. 2013, pp. 1–27. Available online: https://register.geonorge.no/data/documents/Produktspesifikasjoner_FKB-Laser_v1_fkb-laser-v30-2018-01-01_.pdf (accessed on 15 June 2022).

48. Glira, P.; Pfeifer, N.; Mandlburger, G. Rigorous strip adjustment of UAV-based laserscanning data including time-dependent correction of trajectory errors. *Photogramm. Eng. Remote Sens.* **2016**, *82*, 945–954. [CrossRef]

49. Applanix. POS MV OceanMaster. 2019. Available online: https://www.applanix.com/downloads/products/specs/posmv/POS-MV-OceanMaster.pdf (accessed on 10 July 2022).

50. Norbit. NORBIT WINGHEAD i77h. 2020. Available online: https://norbit.com/media/PS-200004-4_WINGHEAD-i77h_A4.pdf (accessed on 10 July 2022).

51. Leica-Geosystems. Leica ScanStation P50. 2017. Available online: https://leica-geosystems.com/products/laser-scanners/scanners/leica-scanstation-p50 (accessed on 10 July 2022).

52. CloudCompare. CloudCompare (Version 2.11.3) [GPL Software]. 2020. Available online: http://www.cloudcompare.org/ (accessed on 1 March 2022).

53. Lague, D.; Brodu, N.; Leroux, J. Accurate 3D comparison of complex topography with terrestrial laser scanner: Application to the Rangitikei canyon (N-Z). *ISPRS J. Photogramm. Remote Sens.* **2013**, *82*, 10–26. [CrossRef]

54. Brasington, J.; Langham, J.; Rumsby, B. Methodological sensitivity of morphometric estimates of coarse fluvial sediment transport. *Geomorphology* **2003**, *53*, 299–316. [CrossRef]

55. Lallias-Tacon, S.; Liébault, F.; Piégay, H. Step by step error assessment in braided river sediment budget using airborne LiDAR data. *Geomorphology* **2014**, *214*, 307–323. [CrossRef]

56. Weber, M.D.; Pasternack, G.B. Valley-scale morphology drives differences in fluvial sediment budgets and incision rates during contrasting flow regimes. *Geomorphology* **2017**, *288*, 39–51. [CrossRef]

57. Wheaton, J.M.; Brasington, J.; Darby, S.E.; Sear, D.A. Accounting for uncertainty in DEMs from repeat topographic surveys: Improved sediment budgets. *Earth Surf. Process. Landf.* **2010**, *35*, 136–156. [CrossRef]

58. Antonarakis, A.S.; Richards, K.S.; Brasington, J. Object-based land cover classification using airborne LiDAR. *Remote Sens. Environ.* **2008**, *112*, 2988–2998. [CrossRef]

59. Crosilla, F.; Macorig, D.; Scaioni, M.; Sebastianutti, I.; Visintini, D. LiDAR data filtering and classification by skewness and kurtosis iterative analysis of multiple point cloud data categories. *Appl. Geomat.* **2013**, *5*, 225–240. [CrossRef]

60. Bulmer, M.G. *Principles of Statistics*; Dover Books: New York, NY, USA, 1979.

61. Glira, P.; Pfeifer, N.; Briese, C.; Ressl, C. A Correspondence Framework for ALS Strip Adjustments based on Variants of the ICP Algorithm. *Photogramm. Fernerkund. Geoinf.* **2015**, *2015*, 275–289. [CrossRef]
62. Skinner, K.D. *Evaluation of LiDAR-Acquired Bathymetric and Topographic Data Accuracy in Various Hydrogeomorphic Settings in the Deadwood and South Fork Boise Rivers, West-Central Idaho, 2007*; U.S. Geological Survey Scientific Investigations Report 2011–5051; U.S. Department of the Interior: Washington, DC, USA, 2011.